

Effects of Ion Energy and Density on the Plasma Etching-Induced Surface Area, Edge Electrical Field, and Multivacancies in MoSe₂ Nanosheets for Enhancement of the Hydrogen Evolution Reaction

Dezhi Xiao, Qingdong Ruan, De-Liang Bao, Yang Luo, Chao Huang, Siying Tang, Jie Shen, Cheng Cheng, and Paul K. Chu*

Plasma functionalization can increase the efficiency of MoSe₂ in the hydrogen evolution reaction (HER) by providing multiple species but the interactions between the plasma and catalyst are not well understood. In this work, the effects of the ion energy and plasma density on the catalytic properties of MoSe₂ nanosheets are studied. The through-holes resulting from plasma etching and multi-vacancies induced by plasma-induced damage enhance the HER efficiency as exemplified by a small overpotential of 148 mV at 10 mA cm⁻² and Tafel slope of 51.6 mV dec⁻¹ after the plasma treatment using a power of 20 W. The interactions between the plasma and catalyst during etching and vacancies generation are evaluated by plasma simulation. Finite element and first-principles density functional theory calculations are also conducted and the results are consistent with the experimental results, indicating that the improved HER catalytic activity stems from the enhanced electric field and more active sites on the catalyst, and reduced bandgap and adsorption energy arising from the etched through-holes and vacancies, respectively. The results convey new fundamental knowledge about the plasma effects and means to enhance the efficiency of catalysts in water splitting as well insights into the design of high-performance HER catalysts.

obtain high-purity hydrogen.^[2] However, constrained by the low efficiency of electrochemical catalysts in the hydrogen evolution reaction (HER) and high cost of noble metals such as Pt, water splitting is still not broadly viable commercially.^[3] To improve the catalytic ability and efficiency, functional catalysts have been synthesized.^[4] 2D transition metal dichalcogenide (TMD) has large potential in HER due to the tunable crystalline and electronic band structures in addition to plenty of active sites for charge exchange and good transport between the catalyst and electrolyte.^[5] Compared to other TMD materials such as MoS₂ and WS₂, MoSe₂ possesses a smaller bandgap and larger interlayer space to facilitate fast charge transfer in HER^[6] and methods to enhance the efficiency include doping and materials engineering.^[7]

As a common industrial technology, plasma functionalization presents a fast and facile way to alter the morphology and structure of nanomaterials by various

plasma-based processes such as etching, doping, and chemical modification.^[8] Plasma modification of TMD catalysts for water splitting has been investigated and plasma-induced defects influence the band structure and charge exchange in the catalytic process.^[7a,9] The Gibbs free energy can be reduced because of produced vacancies by the plasma and ion exposure and the improvement in the catalyst properties is attributed to

1. Introduction

Depletion of traditional fossil fuel and environmental pollution are big concerns of the modern society and sustainable and green energy is highly desirable as a replacement.^[1] In particular, hydrogen is attractive without greenhouse gas emission and water splitting is the most direct method to

Dr. D. Xiao, Dr. Q. Ruan, Dr. Y. Luo, Dr. C. Huang, Dr. S. Tang,
Prof. P. K. Chu
Department of Physics
Department of Materials Science and Engineering, and Department
of Biomedical Engineering
City University of Hong Kong
Tat Chee Avenue, Kowloon, Hong Kong 999077, China
E-mail: paul.chu@cityu.edu.hk

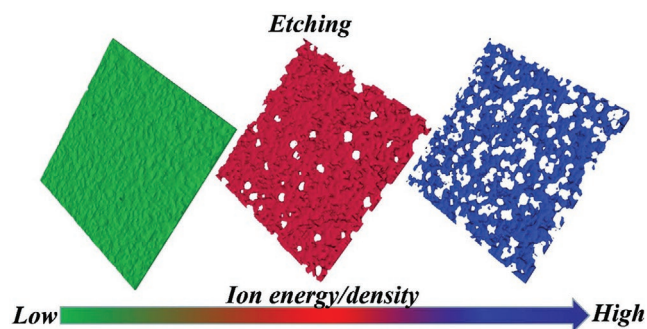
 The ORCID identification number(s) for the author(s) of this article can be found under <https://doi.org/10.1002/sml.202001470>.

DOI: 10.1002/sml.202001470

Dr. D.-L. Bao
Department of Physics and Astronomy
Vanderbilt University
Nashville, TN 37235, USA

Dr. D.-L. Bao
Institute of Physics and University of the Chinese Academy of Sciences
Chinese Academy of Sciences
Beijing 100190, China

Dr. J. Shen, Dr. C. Cheng
Institute of Plasma Physics
Chinese Academy of Sciences
Hefei 230031, China



Scheme 1. Schematic illustration of the effects of different ion energy and density on the plasma etching-induced morphology change of MoSe₂ nanosheet.

vacancies, but the contribution of etched patterns is ignored.^[10] Additionally, the underlying mechanism of the morphological change and vacancy formation in nanomaterials after plasma treatments is still not well understood, especially the interactions between the plasma and catalyst surface. For example, although etching of Bi₂Se₃ films with different gases in Barton's research changes the bandgap and grain boundaries, the mechanisms have not been discussed.^[11] The lack of fundamental understanding has stifled the application of plasma modification to catalysis and it is thus important to study how plasma parameters affect the modification efficacy in addition to an analysis of the cost-effectiveness and process complexity. In this work, a low-pressure capacitively-coupled plasma (CCP) with a distance of 10 cm between two planar electrodes is employed to modify MoSe₂ nanosheets prepared on carbon felt and the effects of the ion energy and flux on the interactions between the plasma and catalyst are investigated by tuning the power of the radio frequency (13.56 MHz) from 10 to 40 W applied to the biased electrode at a fixed pressure of 20 mT and 20 sccm argon flow. After argon plasma functionalization, irregular etched through-holes are randomly distributed on the MoSe₂ nanosheets and the size and number vary with the ion energy and density as demonstrated in **Scheme 1**. Hence, the active sites and electric field can be tailored to optimize the performance of the catalyst. The effects are studied experimentally by scanning electron microscopy (SEM) and theoretically by the finite element method (FEM). The influence of multivacancies induced by plasma-induced damage (PID) because of ion penetration into the catalyst surface is analyzed by transmission electron microscopy (TEM) and the smaller Gibbs free energy (ΔG_H) and smaller bandgap due to multivacancies are corroborated by first-principles density-functional theory (DFT) calculation. By optimizing the ion energy, flux, and angular distribution based on plasma simulation, balanced etching and PID can be accomplished using a power of 20 W to produce the optimal active sites and vacancies for the best HER performance.

2. Results and Discussion

The MoSe₂ nanosheets are synthesized hydrothermally on a piece of carbon felt and treated by the plasma using different

power settings. **Figure 1a** shows the X-ray diffraction (XRD) patterns of the MoSe₂ samples and the diffraction peaks are characteristic of the MoSe₂ crystal and carbon from the carbon felt (**Figure S1**, Supporting Information). In comparison, no evident new peaks are shown in **Figure 1a** meaning that the phase of MoSe₂ is preserved after the plasma treatment. A small increase in the intensity of the (002) peak is observed for a power of 20 W indicating that there is more MoSe₂ irradiated by the X-ray suggesting indirectly more exposed surface. Furthermore, defect formation by the plasma may alter the crystal lattice and produces small shifts in the peaks.^[12] To monitor defect generation, Raman scattering is carried out and as shown in **Figure 1b**, the typical Raman peaks of MoSe₂ are observed revealing A_g¹, E_{2g}¹, and B_{2g}¹.^[5a,6b] The inset in **Figure 1b** shows the details of the A_g¹ peak before and after the plasma treatment. The peak shifts to smaller wavenumbers after the plasma treatment and the largest shift is observed for a plasma power of 20 W. Based on previous reports,^[13] the Raman shift induced by plasma modification can be attributed to defects which change the lattice by stress and strain as well as layer interaction which affects the vibrational frequency by restoring the force between adjacent MoSe₂ layers. However, severe change in the lattice induced by the defects created at a higher ion energy and over-etching by the high ion flux at 40 W as shown in **Scheme 1** can over-extend the stress and strain of lattice and layer interaction. As a result, the largest Raman shift is observed at 20 W by considering the defects and etching effects based on the combination of ion energy and flux.

Defect formation is attributed to PID, which has also been observed from semiconductor fabrication.^[14] The MoSe₂ crystal is disrupted by ion bombardment and Se atoms are etched away forming defects. As a high valence element, the spare Mo atoms supply more electrons and become a donor. Therefore, the defects cause a red-shift in the Raman spectra because of the PID effect and atomic Mo being the donor (Se vacancy). It is also confirmed by the Mott-Schottky measurement (**Figure S2a**, Supporting Information) in which the slope is more positive after the plasma treatment suggesting that the n-type MoSe₂ receives more electrons from the surplus Mo atoms.^[10a] The surface stoichiometry (**Figure S2b**, Supporting Information) further indicates that the ratio of Mo:Se increases after the plasma treatment suggesting that more Se atoms are etched because of the lower surface energy and higher sputtering yield of atomic Se. The effects of defects are determined by X-ray photoelectron spectroscopy (XPS) by analyzing the valence state of MoSe₂. As shown in **Figure 1c**, the peaks of Mo 3d_{5/2} and Mo 3d_{3/2} at 231.8 and 228.7 eV indicate Mo⁴⁺ in MoSe₂.^[5a,6a,b] Compared to the sample without plasma treatment, the appearance of high valence state of Mo⁶⁺ after the plasma treatment indicates that oxygen is incorporated after exposure to air as a result of the dangling bonds of Mo atoms produced after dislodgment of Se atoms,^[10a] especially after the 20 and 40 W treatments (**Figure S3a**, Supporting Information) which create more vacancies by sputtering more Se atoms. However, the valence of Se does not change after the plasma treatment as shown in **Figure 1d** indicating that atomic Se as the vacancy is protected by spare Mo from oxidation. The peaks of Mo 3d and Se 3d shift to higher binding energies by 0.21 eV (**Figure S3b**,

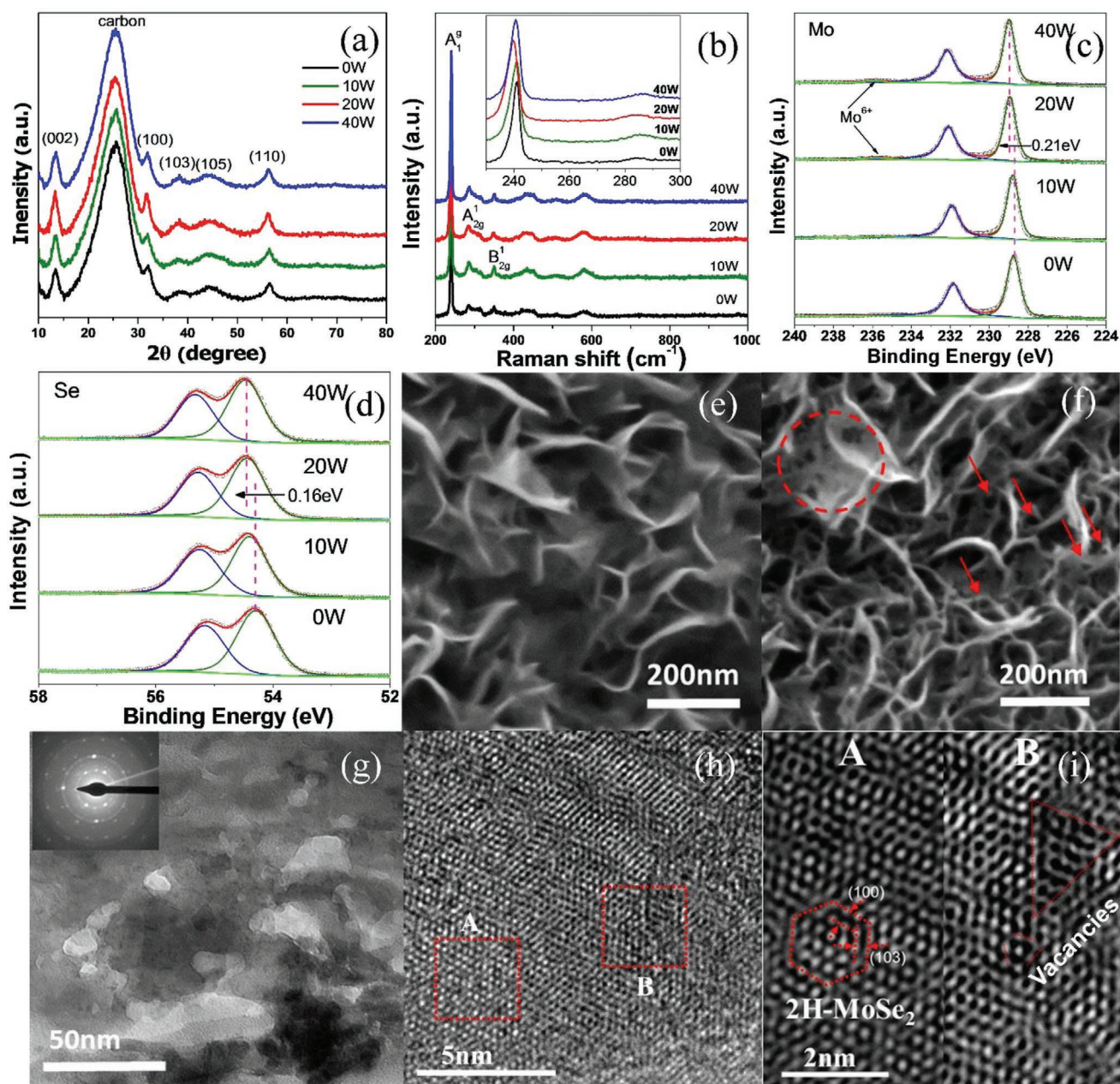


Figure 1. Characterization of MoSe₂ nanosheets on carbon felt. a) XRD pattern and b) Raman scattering spectrum of MoSe₂ treated using different discharge power. XPS spectra of MoSe₂ treated using different power settings. c) Mo 3d and d) Se 3d. SEM images of MoSe₂ treated using e) 0 W and f) 20 W. TEM images of MoSe₂ treated using 20 W. g) Low-resolution TEM image and h,i) High-resolution TEM images.

Supporting Information) and 0.16 eV (Figure S3c, Supporting Information), respectively, suggesting Se vacancy formation and n-type characteristics consistent with the Mott–Schottky measurement.^[10a,11]

The morphological change of the MoSe₂ nanosheets after the plasma treatment is confirmed by SEM. Different from the original structure shown in Figure 1e, the nanosheets are etched by the plasma and ion bombardment and a large number of irregular through-holes are randomly distributed on the nanosheets after the 20 W treatment as shown in Figure 1f. By comparing the features before and after plasma

etching, Figure S4 (Supporting Information) shows that the etched through-holes are observed from both the top and side after the plasma treatment. To further study the ion bombardment effects on the structural change, SEM is used to study the feature changes after the plasma treatment using different power because different ion energy and density are produced. As shown in Figure S5a (Supporting Information), no obvious through-holes are formed for a small power of 10 W compared to the features created by the 20 and 40 W plasma as shown in Figure S4b,c (Supporting Information). Hence, a sufficiently large power is necessary to create through-holes

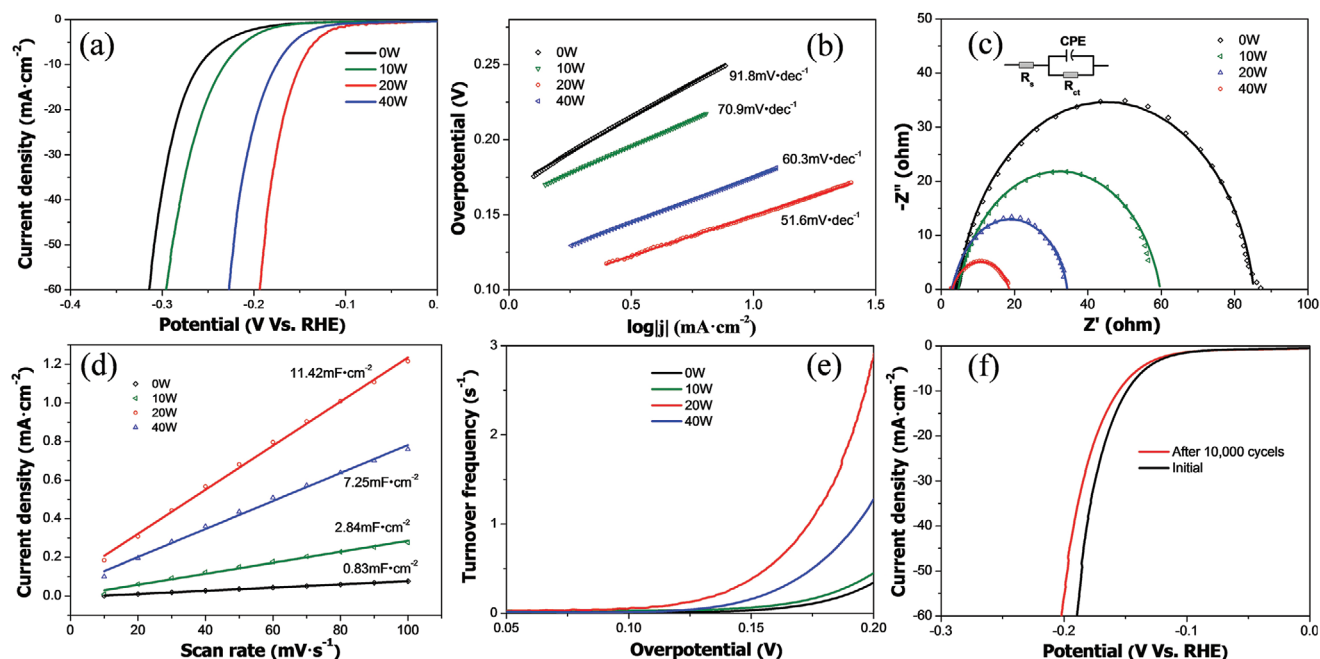


Figure 2. HER characteristics. a) LSV curves. b) Tafel plots. c) Nyquist plots EIS. d) Ratio of current densities at different scanning rates. e) TOFs measurement for MoSe₂ treated using different discharge power. f) LSV comparison before and after 10 000 cycles for MoSe₂ treated using 20 W.

in the nanosheets. The etched through-holes after the 40 W treatment (Figure S5c, Supporting Information) are larger than those after the 20 W treatment (Figure S5b, Supporting Information) showing a positive correlation between etching and plasma power. However, excessively large ion energy and density cause too much etching of catalyst and decrease the effectiveness of the catalyst in HER. Therefore, moderate ion energy and density attained at a power of 20 W produce the optimal through-hole number and size in MoSe₂ nanosheets exposing the most surface which is also confirmed by the BET results in Figure 4a.

The TEM images in Figure S5d (Supporting Information) show the different views and Figure 1g reveals nanosheets with irregular through-holes etched by argon ions. The inset selected-area electron diffraction (SAED) pattern shows the diffraction pattern implying the multicrystal structure of MoSe₂ is fabricated. The surface with a thickness of 3.3 nm consisting of five layers shown in Figure S5e (Supporting Information) indicates a layer spacing of 0.66 nm, which is in line with the theoretical value of 0.65 nm of the MoSe₂(002) plane. The high-magnification TEM (HR-TEM) image in Figure 1i shows the crystal lattices derived from Figure 1h for different areas. The typical crystal structure of 2H-MoSe₂ is observed as faint damage in area A. In comparison, crystal destruction leading to vacancy formation in area B is observed and confirmed by plasma simulation as shown in Figure 3e,f. The blurred crystal structure in contrast to the periodic layers in Figure S5e (Supporting Information) results from PID-induced crystal defects as well. To verify defect formation, the HR-TEM image in Figure S5f (Supporting Information) shows that the lattice is partly damaged and a number of Se atoms are removed forming vacancies.

To determine the effects of plasma functionalization on the catalytic activity of the MoSe₂ nanosheets, the HER characteristics are evaluated electrochemically in 0.5 M H₂SO₄ using a three-electrode configuration. Linear scan voltammetry (LSV) is conducted at a scanning rate of 5 mV s⁻¹ to obtain the polarization curves (Figure 2a). All the potentials are calibrated with respect to the reversible hydrogen electrode (RHE). The MoSe₂ catalyst modified with a power of 20 W delivers the best performance and the potential of -148 mV at 10 mA cm⁻² is better than those of the 10 and 40 W samples. The depressed electrocatalytic activity of the latter is due to either insufficient or excessive plasma treatment in line with the aforementioned characterization results. The Tafel slopes derived from the polarization curves are displayed in Figure 2b and a smaller value of 51.6 mV dec⁻¹ is observed from the 20 W sample suggesting faster kinetics and higher electrocatalytic activity in HER.^[6b] Owing to the larger surface area with etched through-holes and defects induced by PID, there are more abundant redox sites and transfer of protons/electrons is faster between the catalyst and electrolyte, consequently resulting in a smaller overpotential and Tafel slope for the MoSe₂ sample treated with a power of 20 W. Table S1 (Supporting Information) summarizes plasma treated molybdenum-based materials pertaining to the HER activity and our results are better due to the dual effects of defects and etching as a result of the combination of ion energy and flux. The electron transfer process between the catalyst and electrolyte is studied by electrochemical impedance spectroscopy (EIS). Theoretically, a smaller charge transfer resistance (R_{CT}) indicates better and faster proton/electron transfer between the catalyst and electrolyte.^[10e] Figure 2c displays the Nyquist plots in addition to the fitted curves and circuit. The 20 W MoSe₂ sample shows the smallest R_{CT} of

18 Ω than others (88, 60, and 37 Ω , respectively) suggesting better electrical integration and improved conductivity. Direct measurement of the conductivity of the MoSe₂ on carbon felt is conducted using a probing system without an electrolyte.^[9d] As shown in Figure S6 (Supporting Information), lower resistance and higher conductivity are observed from the 20 W MoSe₂ sample demonstrating that plasma functionalization improves not only the electrical integration and conductivity between the catalyst and electrolyte, but also the conductivity of MoSe₂ itself.

To further investigate the intrinsic catalytic properties and electrochemical surface area, the electrochemical double-layer capacitance (C_{dl}) of the solid-liquid interface is calculated by cyclic voltammetry (CV) conducted at different scanning rates from 10 mV to 100 mV s⁻¹ in the potential range between 0.15 and 0.25 V versus RHE (Figure S7, Supporting Information). As shown in the fitted linear plots in Figure 2d, C_{dl} of MoSe₂ for 20 W is 11.42 mF cm⁻² compared to 7.25 mF cm⁻² for 40 W, 2.84 mF cm⁻² for 10 W, and 0.83 mF cm⁻² for the pristine MoSe₂. The results show that the larger electrochemical surface area and superior HER activity arise from more etched through-holes and surface exposed after modification using a plasma power of 20 W. To evaluate the number of catalytic active sites, the turnover frequency (TOF) derived from the polarization curves and C_{dl} are presented in Figure 2e and Figure S8a (Supporting Information), indicating that the 20 W sample has the most active sites as well. According to the electrochemical measurements, the plasma functionalizes MoSe₂ by creating etched through-holes and multivacancies for enhancement of HER. The better performance stems from the improved active sites and conductivity, especially the 20 W sample processed with the proper ion energy and plasma density. The stability of the 20 W MoSe₂ sample is evaluated by comparing the LSV curves before and after 10 000 cycles. The long-term stability is assessed by chronoamperometry in which a graphite rod replaces the Pt/C electrode to avoid Pt/C dissolution and contamination to other electrodes. Only small deterioration is observed after 10 000 cycles (Figure 2f) and long-term stability is established by the 20 h test (Figure S8b, Supporting Information).

In spite of the good outcome in the HER activity after the plasma treatment, the mechanism and effects of different plasma parameters are not well known.^[7a,9a,10b,c] The plasma density and ion energy play important roles in etching and PID accompanies ion bombardment and plasma exposure.^[15] To investigate the interactions between the plasma and catalyst, plasma simulation is carried out to determine the ion density and energy distribution in the plasma. The discharge parameters are described in Figure S9 (Supporting Information) in which the discharge voltage (radio frequency of 13.56 MHz) produced by the power is applied to the electrode to generate the plasma. Although a series of complicated reactions are involved in the plasma discharge, the main reactions are summarized in Table S2 (Supporting Information) for plasma simulation. **Figure 3a** displays the density distribution of argon ions along the central axis of the chamber under different power. The discharge using 20 W shows a medium value compared to the larger and smaller densities for 40 and 10 W and the characteristic drop implies sheath formation on the electrode.^[16] The ion flux to the electrode surface affects etching as shown in

Figure 3b and the 20 W plasma discharge supplies a moderate amount of ions to interact with the catalyst. On account of the plasma sheath on the electrode surface (Figure S10a, Supporting Information), ions are accelerated through the sheath (Figure S10b, Supporting Information) and the ion energy distribution (IED) varies with the position and power in the sheath.^[15b,17] As shown by the ion energy and angular distribution (IEAD) at different positions above the electrode surface in Figure 3c, evolution of the IEAD illustrates that the ion energy is low and dispersive before entering the sheath at a distance of 20 mm above the electrode surface (80 mm in Figure 3a). It shows an acceleration tail at 15 mm and finally attains the balanced ion energy in the sheath at 8 mm above the electrode. Figure 3d and Figure S9c (Supporting Information) present the IEAD and IED above the electrode surface for different power, indicating that a higher power creates an ion energy distribution with a smaller angle but larger energy in a broad range. The IEAD and IED at different positions and power show that ions are accelerated in the sheath and attain the maximum energy for effective etching, and the ion energy at a higher power tends to be higher and more intensive for ion bombardment inducing more severe PID.

Etching simulation is carried out by taking into account the ion flux, IEAD and IED obtained from the above calculation to evaluate the etching and PID effects. As shown in Figure 3e, irregular through-holes are randomly etched in the nanosheets together with extensive damage due to sputtering by argon ions at 20W and the results are consistent with the features in Figure 1g. Assessment of vacancies induced by PID is shown in Figure 3f which estimates the contribution of each ion to vacancy formation. The damage mainly occurs on the surface within a limited penetrating depth of less than 2.5 nm and a large number of vacancies could be created by the ion flux calculated in Figure 3b. Compared with the thickness of MoSe₂ nanosheet estimated in Figure S11 (Supporting Information), the damage thickness is relatively small,^[14a,18] implying that the main MoSe₂ properties do not change. The defects of vacancies produced on the surface enhances the HER activity by accelerating electron transfer between the catalyst and electrolyte as a result of the reduced bandgap and absorption energy of vacancies as shown in Figure 4. The ion bombardment distribution in the nanosheets for an energy of 150 eV (20 W power) is presented in Figure S10d (Supporting Information) in which the vacancy evolution through the removal of atoms by ions is revealed. The interactions between the plasma and catalyst produce etched through-holes and PID defects are confirmed by plasma simulation. Combining the SEM and plasma simulation results, excessively small or large ion energy and flux do not deliver the optimal performance due to insufficient defects of vacancies and etched through-holes produced at 10 W and over-etching produced at 40 W leading to removal of catalyst as shown in Scheme 1. By considering the plasma simulation results for different ion energies, densities, etching and vacancies, the plasma discharge sustained by a power of 20 W produces the optimal ion density and ion energy for HER.

In order to evaluate the contribution of the morphological change to the HER catalytic activity, the electric field and protons around the catalyst surface are investigated by FEM^[19] to study the electron/proton transfer efficiency. FEM simulation

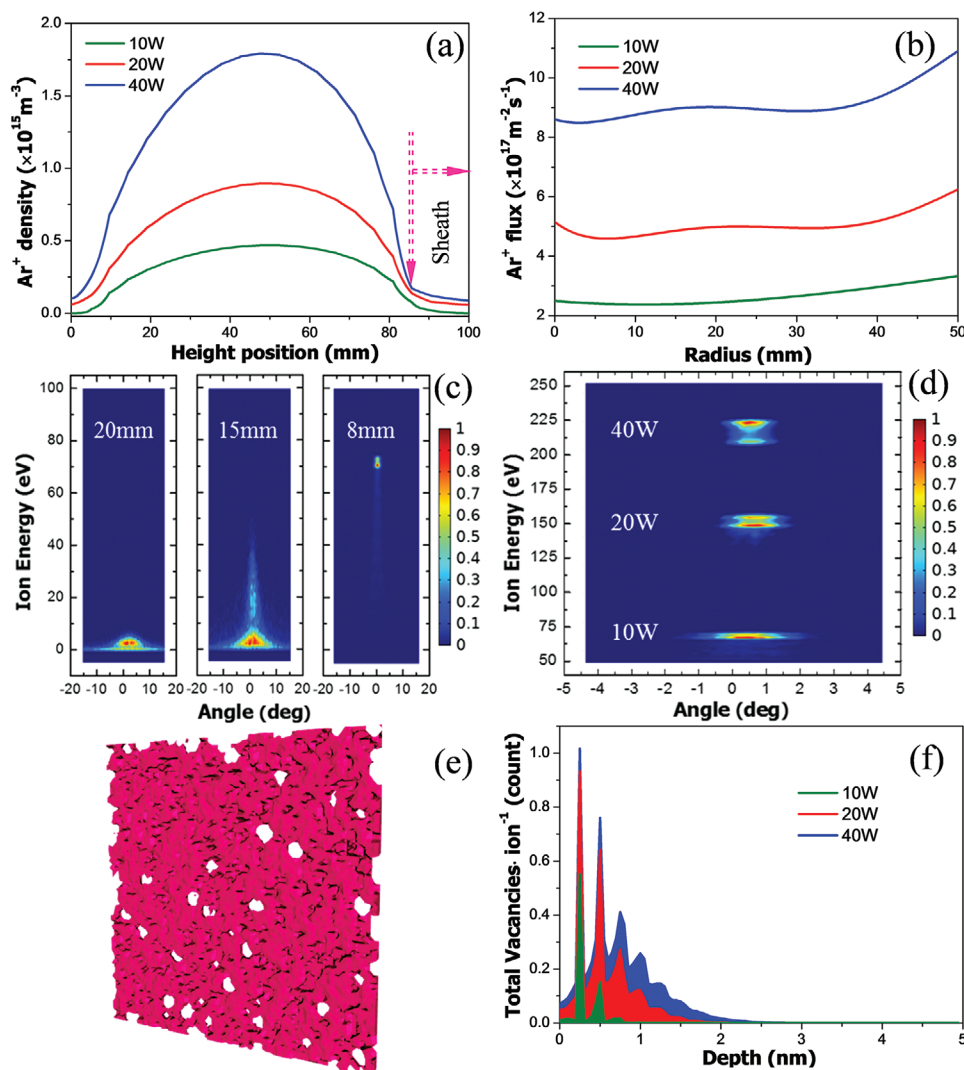


Figure 3. Plasma simulation. a) Electron density distribution and b) Ion flux on the electrode surface for different discharge power. c) Evolution of IED and IEAD at different positions above the electrode. d) Evolution of IED and IEAD for different discharge power on the electrode surface. e) Etching pattern using 20 W discharge. f) Vacancies distribution on the MoSe₂ surface induced by PID.

is conducted based on some assumptions shown in Figure S12 (Supporting Information). A small decrease of 0.01 V is observed (Figure S13a, Supporting Information) because of voltage delivery in the MoSe₂ and significant enhancement in the electric field occurs on the edge of the nanosheets as shown in Figure S13b (Supporting Information). Plasma etching changes not only the structure, but also the physical properties. As shown in Figure 4b,c, the channel formed in the through-hole exposes more surface and increases the Brunauer–Emmett–Teller (BET) area as shown in **Figure 4a**. However, over-etching removes too much catalyst as shown in Figure 4c leading to a decrease of BET and an increase in the average pore diameter as exemplified by the 40 W sample in Figure 4a. Besides surface exposure, the electric field on the edge of the through-hole is enhanced as shown in Figure 4b,c and the enhancement is also displayed in Figure S13d (Supporting Information) for the positions in Figure S13c (Supporting Information). To corroborate the edge electric field effect, the

comparison between simulation and SEM image with improved contrast is presented in Figure S13e,f (Supporting Information).^[20] The edges of the through-holes and nanosheets in Figure S13e (Supporting Information) exhibit a similar effect to those marked in Figure S13f (Supporting Information) with a sharp electric field. Hence, the etched through-holes contribute to the increase in the BET as well as enhancement of the electric field. Proton adsorption on the catalyst surface is calculated to evaluate electron/proton transfer.^[19b,c] The electric field distribution in the electrolyte (Figure S14a, Supporting Information) indicates the movement of protons and H⁺ is attracted and accelerated to the catalyst surface under a stronger electric field as shown in Figure S14b (Supporting Information). The H⁺ adsorption calculation in Figure S13c,d (Supporting Information) demonstrates that H⁺ is extensively absorbed on the edge of the through-holes.

To evaluate the defects induced by PID, vacancy generation in MoSe₂ is investigated by electron spin resonance spectroscopy

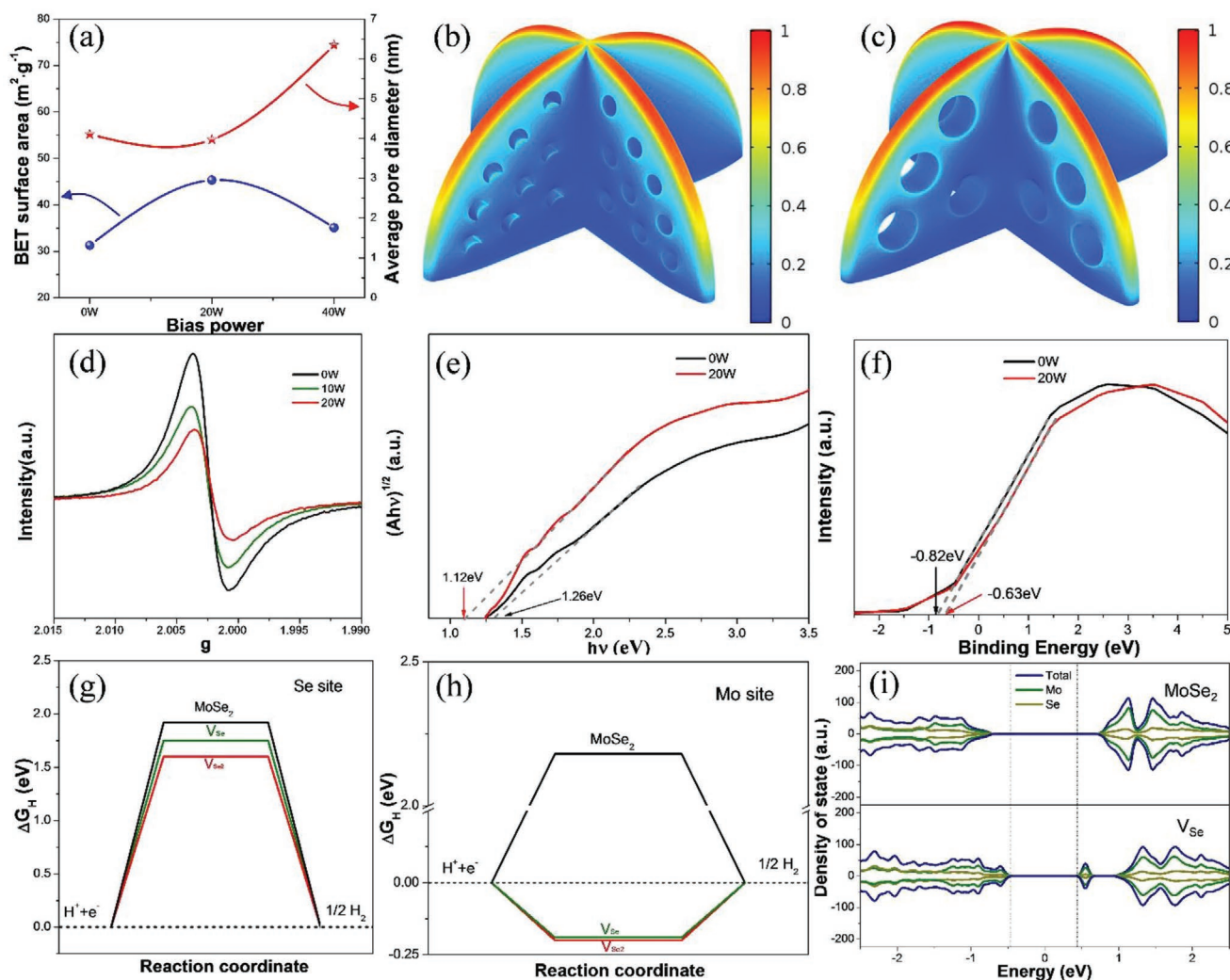


Figure 4. Analysis of MoSe₂ treated using different discharge power. a) BET analysis, b) Normalized electric field distribution on the MoSe₂ surface treated using 20 W. c) Normalized electric field distribution on the MoSe₂ surface treated using 40 W. d) ESR spectra. e) Estimated bandgap derived by UV-vis spectrophotometry. f) VBM derived from XPS; Plots of ΔG_{H} for hydrogen adsorption on g) Mo Site, h) Se site for the different cases; i) DOS of the pristine MoSe₂ and MoSe₂ with V_{Se} .

(ESR) to provide fingerprint paramagnetic signals.^[21] As shown in Figure 4d, the sharp peak at $g \approx 2.0$ can be ascribed to resonance from Mo–Se dangling bonds and a smaller intensity indicates more Se vacancies. The results are in line with the calculation in Figure 3f. As summarized in Table S3 (Supporting Information), since Se atoms can be removed more easily than Mo atoms by ion bombardment because of the lower surface energy of atomic Se, Se vacancies are produced accompanying the formation of etched through-holes and 14.8% defects are estimated by XPS. UV-vis spectroscopy (Figure S15, Supporting Information) is carried out to estimate the band energy change due to the defects.^[22] Compared to the pristine MoSe₂ (1.26 eV), the bandgap (1.12 eV) of MoSe₂ with vacancies is smaller as shown in Figure 4e reflecting better conductivity and faster electron transfer.^[10a,22] The closer (≈ 0.19 eV) of the valence band maximum (VBM) to the Fermi level estimated by XPS in Figure 4f confirms easier electron transfer.^[11] To further understand the contribution of vacancies to the catalytic activity,

DFT calculation is performed based on the vacancies observed from the MoSe₂ basal plane shown in Figure S16a (Supporting Information) to investigate Se vacancy (V_{Se}) and Se₂ vacancy (V_{Se_2}) formation. The ΔG_{H} calculation for H⁺ adsorption in Figure 4g,h and Table S4 (Supporting Information) disclose that MoSe₂ with vacancies has smaller ΔG_{H} on both the Mo and Se sites, indicating superior H⁺ adsorption surface after plasma functionalization.^[6c,10a,22] Moreover, the smaller $|\Delta G_{\text{H}}|$ on the Mo site for both V_{Se} and V_{Se_2} arises from Mo atoms supplying electrons to H⁺ as revealed by the Mott–Schottky measurement (Figure S2a, Supporting Information). Comparison of the density of states (DOS) between the pristine MoSe₂ and MoSe₂ with Se vacancies in Figure 4i and Figure S16b (Supporting Information) shows new states mainly arising from the Mo states near the Fermi level for the case of Se vacancies. The results show not only abundant Mo atoms released for H⁺ transformation, but also decreased bandgap and conductivity improvement consistent with the results in Figure 4e and EIS in Figure 2c.

In accordance with the VBM estimated in Figure 4f, the calculation in Figure 4i indicates the VBM shift to the Fermi level benefits electron transfer.

Received: March 6, 2020
Revised: April 24, 2020
Published online: May 28, 2020

3. Conclusion

MoSe₂ nanosheets are prepared on carbon felt and modified by the CCP plasma using different ion energies and densities to promote the HER performance of the catalyst. Enhanced HER capability with a lower overpotential of 148 mV at 10 mA cm⁻² and smaller Tafel slope of 51.6 mV dec⁻¹ is observed after the 20 W plasma treatment using the proper ion density and energy. A larger ion density and higher ion energy in the plasma produce a larger ion flux for etching and more severe bombardment-induced damage (defects). Our results reveal that a moderate ion density and energy yield balanced etching effects and defects for the best HER characteristics. Plasma simulation discloses the evolution of the plasma discharge to better understand and control the interactions between the plasma and catalyst. The etching process simulated by FEM enhances the electric field and active sites around the catalyst surface giving rise to stronger adsorption of H⁺ and faster electron transfer. The abundant Se vacancies generated by PID render more Mo atoms as donors to supply electrons for H⁺ transformation. DFT calculation reveals that the vacancies in MoSe₂ not only improve the conductivity by decreasing the bandgap, but also produce a smaller ΔG_H resulting in easier absorption of H⁺. The experimental and simulation results demonstrate that the morphological change and vacancies created by plasma etching and PID promote the HER activity by increasing the activated electrocatalytic sites, conductivity, as well as H⁺ absorption capacity. The results provide a better understanding of the interactions between the plasma and catalyst and the effectiveness of plasma processing on surface functionalization of catalysts for high-efficiency water splitting.

Supporting Information

Supporting Information is available from the Wiley Online Library or from the author.

Acknowledgements

This work was financially supported by the Hong Kong Scholars Program (XJ2018009) and City University of Hong Kong Strategic Research Grant (SRG) No. 7005105.

Conflict of Interest

The authors declare no conflict of interest.

Keywords

edge electric field, etched through-holes, hydrogen evolution reaction, multivacancies, plasma simulation, plasma-induced damage

- [1] S. M. Chu, A. Majumdar, *Nature* **2012**, *488*, 294.
- [2] a) V. R. Stamenkovic, D. Strmcnik, P. P. Lopes, N. M. Markovic, *Nat. Mater.* **2017**, *16*, 57; b) J. A. Turner, *Science* **2004**, *305*, 972.
- [3] a) X. Zou, Y. Zhang, *Chem. Soc. Rev.* **2015**, *44*, 5148; b) J. Zhang, T. Wang, P. Liu, Z. Liao, S. Liu, X. Zhuang, M. Chen, E. Zschech, X. Feng, *Nat. Commun.* **2017**, *8*, 15437; c) Q. Wu, M. Luo, J. Han, W. Peng, Y. Zhao, D. Chen, M. Peng, J. Liu, F. M. F. de Groot, Y. Tan, *ACS Energy Lett.* **2020**, *5*, 192.
- [4] a) Z. W. Seh, J. Kibsgaard, C. F. Dickens, I. Chorkendorff, J. K. Norskov, T. F. Jaramillo, *Science* **2017**, *355*, eaad4998; b) M. S. Fabera, J. Song, *Energy Environ. Sci.* **2014**, *7*, 3519.
- [5] a) Y. Qu, H. Medina, S. W. Wang, Y. C. Wang, C. W. Chen, T. Y. Su, A. Manikandan, K. Wang, Y. C. Shih, J. W. Chang, H. C. Kuo, C. Y. Lee, S. Y. Lu, G. Shen, Z. M. Wang, Y. L. Chueh, *Adv. Mater.* **2016**, *28*, 9831; b) Q. Gao, W. Zhang, Z. Shi, L. Yang, Y. Tang, *Adv. Mater.* **2019**, *31*, 1802880; c) Q. Lu, Y. Yu, Q. Ma, B. Chen, H. Zhang, *Adv. Mater.* **2016**, *28*, 1917; d) A. Eftekhari, *Int. J. Hydrogen Energy* **2017**, *42*, 11053.
- [6] a) D. Xiao, C. Huang, Y. Luo, K. Tang, Q. Ruan, G. Wang, P. K. Chu, *ACS Appl. Mater. Interfaces* **2020**, *12*, 2460; b) L. Najafi, S. Bellani, R. Oropesa-Nuñez, A. Ansaldo, M. Prato, A. E. Del Rio Castillo, F. Bonaccorso, *Adv. Energy Mater.* **2018**, *8*, 1801764; c) R. K. Biroju, D. Das, R. Sharma, S. Pal, L. P. L. Mawlong, K. Bhorkar, P. K. Giri, A. K. Singh, T. N. Narayanan, *ACS Energy Lett.* **2017**, *2*, 1355.
- [7] a) S. Dou, L. Tao, R. Wang, S. El Hankari, R. Chen, S. Wang, *Adv. Mater.* **2018**, *30*, 1705850; b) B. Yao, J. Zhang, X. Fan, J. He, Y. Li, *Small* **2019**, *15*, 1803746.
- [8] a) G. S. Oehrlein, R. J. Phaneuf, D. B. Graves, *J. Vac. Sci. Technol., B: Nanotechnol. Microelectron.: Mater., Process., Meas., Phenom.* **2011**, *29*, 010801; b) V. M. Donnelly, A. Kornblit, *J. Vac. Sci. Technol., A* **2013**, *31*, 050825; c) H. C. Wang, Y. C. Lin, C. H. Chen, C. H. Huang, B. Chang, Y. L. Liu, H. W. Cheng, C. S. Tsao, K. H. Wei, *Nanoscale* **2019**, *11*, 17460; d) Z. Bo, S. Mao, Z. J. Han, K. Cen, J. Chen, K. K. Ostrikov, *Chem. Soc. Rev.* **2015**, *44*, 2108; e) Z. Bo, S. Yang, J. Kong, J. Zhu, Y. Wang, H. Yang, X. Li, J. Yan, K. Cen, X. Tu, *ACS Catal.* **2020**, *10*, 4420.
- [9] a) H. Liang, F. Ming, H. N. Alshareef, *Adv. Energy Mater.* **2018**, *8*, 1801804; b) V. T. Nguyen, T. Y. Yang, P. A. Le, P. J. Yen, Y. L. Chueh, K. H. Wei, *ACS Appl. Mater. Interfaces* **2019**, *11*, 14786; c) S. Mao, Z. Wen, S. Ci, X. Guo, K. K. Ostrikov, J. Chen, *Small* **2015**, *11*, 414; d) C.-C. Cheng, A.-Y. Lu, C.-C. Tseng, X. Yang, M. N. Hedhili, M.-C. Chen, K.-H. Wei, L.-J. Li, *Nano Energy* **2016**, *30*, 846.
- [10] a) B. Xia, T. Wang, X. Jiang, T. Zhang, J. Li, W. Xiao, P. Xi, D. Gao, D. Xue, J. Ding, *ACS Energy Lett.* **2018**, *3*, 2167; b) W. Chen, Y. Zhang, G. Chen, R. Huang, Y. Zhou, Y. Wu, Y. Hu, K. Ostrikov, *J. Mater. Chem. A* **2019**, *7*, 3090; c) Y. Guo, T. Wang, J. Chen, J. Zheng, X. Li, K. K. Ostrikov, *Adv. Energy Mater.* **2018**, *8*, 1800085; d) L. Xu, Q. Jiang, Z. Xiao, X. Li, J. Huo, S. Wang, L. Dai, *Angew. Chem., Int. Ed.* **2016**, *55*, 5277; e) D. Zhou, X. Xiong, Z. Cai, N. Han, Y. Jia, Q. Xie, X. Duan, T. Xie, X. Zheng, X. Sun, X. Duan, *Small Methods* **2018**, *2*, 1800083; f) K. Chen, A. Roy, A. Rai, A. Valsaraj, X. Meng, F. He, X. Xu, L. F. Register, S. Banerjee, Y. Wang, *ACS Appl. Mater. Interfaces* **2018**, *10*, 1125.
- [11] A. T. Barton, L. A. Walsh, C. M. Smyth, X. Qin, R. Addou, C. Cormier, P. K. Hurley, R. M. Wallace, C. L. Hinkle, *ACS Appl. Mater. Interfaces* **2019**, *11*, 32144.
- [12] M. Lang, C. L. Tracy, R. I. Palomares, F. Zhang, D. Severin, M. Bender, C. Trautmann, C. Park, V. B. Prakapenka, V. A. Skuratov, R. C. Ewing, *J. Mater. Res.* **2015**, *30*, 1366.

- [13] a) P. V. Mwonga, R. Barik, S. R. Naidoo, A. Quandt, K. I. Ozoemena, *Phys. Chem. Chem. Phys.* **2018**, *20*, 28232; b) J. Jadwiszczak, C. O'Callaghan, Y. Zhou, D. S. Fox, E. Weitz, D. Keane, C. P. Cullen, I. O'Reilly, C. Downing, A. Shmeliov, P. Maguire, J. J. Gough, C. McGuinness, M. S. Ferreira, A. L. Bradley, J. J. Boland, G. S. Duesberg, V. Nicolosi, H. Zhang, *Sci. Adv.* **2018**, *4*, eaao5031.
- [14] a) K. Eriguchi, *J. Phys. D: Appl. Phys.* **2017**, *50*, 333001; b) A. Matsuda, Y. Nakakubo, Y. Takao, K. Eriguchi, K. Ono, *Thin Solid Films* **2010**, *518*, 3481.
- [15] a) D. J. Economou, *J. Phys. D: Appl. Phys.* **2014**, *47*, 303001; b) A. Agarwal, M. J. Kushner, *J. Vac. Sci. Technol., A* **2008**, *26*, 498; c) E. C. Neyts, K. K. Ostrikov, M. K. Sunkara, A. Bogaerts, *Chem. Rev.* **2015**, *115*, 13408.
- [16] a) S. Robertson, *Plasma Phys. Controlled Fusion* **2013**, *55*, 093001; b) D. J. Economou, *Plasma Processes Polym.* **2017**, *14*, 1600152.
- [17] Y. Zhang, M. J. Kushner, N. Moore, P. Pribyl, W. Gekelman, *J. Vac. Sci. Technol., A* **2013**, *31*, 061311.
- [18] V. Martirosyan, O. Joubert, E. Despiou-Pujo, *J. Phys. D: Appl. Phys.* **2019**, *52*, 055204.
- [19] a) J. Ding, E. Strelcov, S. V. Kalinin, N. Bassiri-Gharb, *Nano Lett.* **2015**, *15*, 3669; b) M. Kang, D. Perry, C. L. Bentley, G. West, A. Page, P. R. Unwin, *ACS Nano* **2017**, *11*, 9525; c) M. Liu, Y. Pang, B. Zhang, P. De Luna, O. Voznyy, J. Xu, X. Zheng, C. T. Dinh, F. Fan, C. Cao, F. P. de Arquer, T. S. Safaei, A. Mepham, A. Klinkova, E. Kumacheva, T. Filleter, D. Sinton, S. O. Kelley, E. H. Sargent, *Nature* **2016**, *537*, 382.
- [20] a) M. M. E. Gomati, M. Prutton, B. Lamb, C. G. Tuppen, *Surf. Interface Anal.* **1988**, *11*, 251; b) E. Alexander, L. Thomas, N. Gert, *J. Microsc.* **2007**, *228*, 110.
- [21] a) C. Dai, E. Qing, Y. Li, Z. Zhou, C. Yang, X. Tian, Y. Wang, *Nanoscale* **2015**, *7*, 19970; b) Y. Yin, J. Han, Y. Zhang, X. Zhang, P. Xu, Q. Yuan, L. Samad, X. Wang, Y. Wang, Z. Zhang, P. Zhang, X. Cao, B. Song, S. Jin, *J. Am. Chem. Soc.* **2016**, *138*, 7965.
- [22] S. Deng, Y. Zhong, Y. Zeng, Y. Wang, Z. Yao, F. Yang, S. Lin, X. Wang, X. Lu, X. Xia, J. Tu, *Adv. Mater.* **2017**, *29*, 1700748.